Optical properties of planar metallic photonic crystal structures: Experiment and theory

A. Christ,* T. Zentgraf, and J. Kuhl
Max-Planck-Institut für Festkörperforschung, 70569 Stuttgart, Germany

S. G. Tikhodeev and N. A. Gippius
A. M. Prokhorov General Physics Institute RAS, Vavilova 38, Moscow 119991, Russia

H. Giessen
Institute of Applied Physics, University of Bonn, 53115 Bonn, Germany
(Received 14 April 2004; revised manuscript received 11 June 2004; published 28 September 2004)

We report on results of transmission measurements of metallic nanowire arrays deposited on top of different dielectric substrates. The appearance of grating anomalies, which critically depend on the substrate thickness, provides evidence that the optical response of these planar metallic photonic crystal structures can be strongly modified. While only Rayleigh-type anomalies are observed for thin dielectric substrates, thicker waveguiding substrates can induce strong coupling phenomena. This strong coupling results in the formation of waveguide-plasmon polaritons with a large Rabi splitting up to 250 meV. We show that the coupling phenomena vary with the nanowire grating period, the angle of incidence, and also the waveguide layer thickness. A scattering-matrix-based numerical method is used to calculate the transmission properties and the near-field spatial distributions of such metallic photonic crystal structures. All experimental results are well confirmed by our theoretical calculations.

DOI: 10.1103/PhysRevB.70.125113 PACS number(s): 78.66.−w, 42.70.Qs, 73.20.Mf

I. INTRODUCTION

The exceptional optical properties of nanostructured materials have been the subject of extensive research activities in recent years. It has been shown that spatial structuring on a sub-micrometer scale can strongly change the light-matter interaction if compared with the properties of a macroscopically homogeneous material. Especially the well-known photonic crystal structures[1–3] exhibit a rich variety of important optical phenomena which already have inspired the development of various nanooptical devices for future technical applications. Initially, such photonic crystal structures were mainly built of transparent dielectric materials with a distinct difference of their refractive indices. However, nowadays considerable effort is devoted to the investigation of *polaritonic* photonic crystal structures with complex unit cells, containing nanostructured semiconducting or metallic materials.[4–8] Such polaritonic crystals are particularly attractive because of their ability to control electronic and photonic resonances simultaneously. Therefore, such structures may open up further impressive possibilities for tailoring the light-matter interaction.

Various photonic crystal structures with nanostructured metals have been realized so far. In addition to periodically modulated metal surfaces, including surface corrugation[9,10] and hole arrays,[11] especially regular arrangements of individual metal nanoparticles on dielectric substrates[12] are prominent examples of such polaritonic crystal structures. Large photonic band gaps,[13] extraordinary light transmission properties,[11] negative refraction,[14] and strong coupling effects between electronic and photonic resonances[15] have been demonstrated. The particular optical properties of these metallic nanostructures can be attributed to the excitation of so-called particle or surface plasmons.[16] These electronic excitations are a consequence of the collective oscillation of the conduction band electrons in the metal. They manifest themselves in strong field enhancement near the metal surface.

Like more complex two- or three-dimensionally periodic structures,[17] also planar metal gratings which are based on a periodic one-dimensional (1D) arrangement of individual metallic nanowires can be interpreted as 1D metallic photonic crystal slabs (PCS). It is obvious that different interaction phenomena have to be taken into account for a detailed analysis of such PCS. The investigation of these interaction phenomena seems to be quite important, especially with regard to the nature of inter-particle-plasmon interaction in future plasmonic nanodevices (e.g., three-dimensional metallic photonic crystals or surface plasmon polariton grating couplers). In contrast to isolated metal nanoparticles[18–20] or nanowires, the optical response of a periodic arrangement of individual metal nanostructures (dots or wires) will be influenced by near- and far-field coupling effects. While shifts of the particle plasmon resonance[21] and extended plasmon modes have been found for contiguous particles[22] with $d \sim a$ (where d is the distance between the nanostructures and a is their characteristic size, e.g., the nanowire width), far-field coupling effects will dominate the optical properties of planar photonic crystals with a periodicity on a length scale $d > a$ and comparable to the wavelength of light.[23] In addition to works on randomly distributed metallic nanoparticles,[24] it has been recently shown that the interaction between photonic and electronic resonances of ordered structures can lead to very pronounced modifications of their optical response.[12,15] Another similar example of such interaction phenomena is the interplay between localized and extended surface plasmon resonances of periodic hole arrays in metallic films.

In this paper, we give an extended analysis of the far-field effects observed in periodic gold nanowire arrays with periods $d > a$, exceeding the near-field coupling regime. We ex-

perimentally and theoretically demonstrate that the collective interaction of the nanowires with the light field leads to interesting diffraction phenomena which strongly modify the optical properties of the nanowires with respect to the single-nanowire case. The described phenomena can be related to the appearance of so-called Wood anomalies[25] which are intrinsic properties of photonic crystal slabs. The signatures of two types of Wood anomalies can be found in the transmission spectra of PCS, both types associated with waves exited by the incoming light and propagating along the periodic structure. Metal nanowire gratings on dielectric substrates show diffractive Wood anomalies (also called Rayleigh anomalies) which are associated with the opening of new diffraction orders either into air or into the substrate with the increase of the incoming photon energy.[26] If a waveguiding layer is added below the grating structure, additional resonance effects (waveguiding anomalies; see, e.g., Ref. 28 and references therein) will appear. By changing the geometrical properties of the metallic photonic crystal and therefore influencing for instance the spectral overlap of the particle plasmon resonance and the grating anomaly, we show that both effects can lead to dramatic changes of the individual particle plasmon resonances.[27] It is worth mentioning that, in principle, all phenomena reported in this work also occur for two-dimensional gold nanocluster arrays deposited on top of dielectric substrates. However, the nanowire structure is advantageous for highlighting the observed phenomena. Besides a larger oscillator strength of the nanowire plasmons, the possibility to turn off the nanowire plasmon resonance is quite instructive. For light polarization parallel to the nanowires, no particle plasmons can be excited, and we can clearly identify the pure uncoupled grating anomalies.

The structure of the paper is as follows. In Sec. II, we describe our metal nanowire structures and the experimental setup. In Sec. III, we give a short overview of the scattering-matrix-based numerical method which is used for modelling of our experimental results. In Sec. IV, the optical properties of metal nanowire gratings deposited on top of a non-waveguiding substrate are discussed. The results show clear evidence of Rayleigh-type anomalies in accordance with the theoretical predictions. In contrast, in Sec. V we concentrate on nanowire structures deposited on top of thicker dielectric waveguiding layers. Strong coupling between optical modes and plasmon resonances is observed for these structures, and the experimental data are well reproduced by the theory. The calculated near-field spatial distributions will be discussed in this section. Finally, a summary of all findings is given in Sec. VI.

II. SAMPLES AND EXPERIMENTAL TECHNIQUES

Figure 1 displays a schematic view of our sample structure. One-dimensional gold nanowire gratings were prepared by electron beam lithography on top of indium tin oxide (ITO) layers deposited on a quartz substrate. For all experimental investigations, the nanowire width of 100 nm and the nanowire height of 20 nm were kept fixed, while the nanowire periods were varied between $d_x = 350$ nm and 600 nm. The possible grating extensions were restricted to 100 $\times 100\ \mu m^2$ due to limitations of the electron beam writing system. Two slightly modified sample geometries have to be taken into account for the comprehensive analysis of the fundamental optical properties of these metallic photonic crystal structures. While samples with an ITO layer thickness of $L_z = 15$ nm were used for experiments concerning Rayleigh-type phenomena, resonant coupling effects were only observed for thicker ITO films, supporting guided modes. Therefore samples with a 140-nm-thick ITO waveguiding layer were produced.

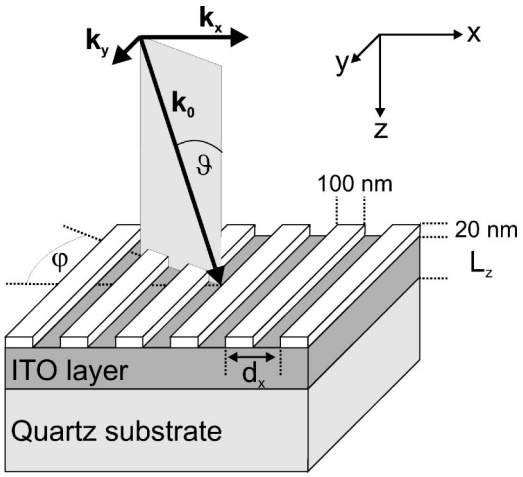

FIG. 1. Schematic view of the gold nanowire array on top of an ITO layer. Samples with different ITO thicknesses are investigated ($L_z = 15$ nm or $L_z = 140$ nm). Angle- and polarization-dependent transmission measurements are possible.

A conventional white light (halogen lamp) transmission setup was used for recording all extinction spectra. The samples were mounted on a rotation stage so that angle dependent measurements were possible. Besides the angle of incidence, also a distinct light polarization could be selected. Experiments with polarization parallel or perpendicular to the nanowires have been performed. It is important to remark that precise measurements of these fine spectral features require a careful adjustment of the setup. Special care has to be taken on the light aperture angle which has turned out to be a sensitive parameter. It has been shown that an aperture below 0.2° is necessary for reasonably exact measurements. In our experiments this requirement was achieved by placing a 100 μm pinhole into the transmitted and recollimated white light beam.

III. SCATTERING-MATRIX BASED THEORETICAL DESCRIPTION

We employed the scattering matrix method[28–30] for the theoretical description of the optical properties of the photonic crystal slab. We focus on the main points as the method itself has been extensively described in Ref. 28. The incoming light with frequency ω and wavevector,

$$\mathbf{k} = (k_x, k_y, k_z) = k_0(\sin\vartheta\cos\varphi, \sin\vartheta\sin\varphi, \cos\vartheta), \quad (1)$$

(where $k_0 = \omega/c$, and ϑ and φ are the polar and azimuthal angles of incidence, respectively; see Fig. 1) is treated as a

planar incoming wave with electric and magnetic fields $(\mathbf{E},\mathbf{H}) \propto \exp(i\mathbf{kr} - i\omega t)$ far away from the structure on the vacuum side, $z < 0$.

The 1D periodic structure couples this incoming wave, the main harmonic, with all Bragg harmonics outgoing into vacuum and substrate. The reflected main harmonic ($g=0$) and the diffracted and evanescent harmonics ($g = \pm 1, \pm 2, \ldots, \pm G$) into the vacuum are

$$\mathbf{k}_g^{\mathrm{out,vac}} = (k_{g,x}, k_y, -k_{g,z}^{\mathrm{vac}}) = \left(k_x + \frac{2\pi g}{d_x}, k_y, - \sqrt{k_0^2 - \left(k_x + \frac{2\pi g}{d_x} \right)^2 - k_y^2} \right). \quad (2)$$

The transmitted main harmonic and the diffracted and evanescent harmonics into the substrate are

$$\mathbf{k}_g^{\mathrm{out,sub}} = (k_{g,x}, k_y, k_{g,z}^{\mathrm{sub}}) = \left(k_x + \frac{2\pi g}{d_x}, k_y, \sqrt{k_0^2 \varepsilon_{\mathrm{sub}} - \left(k_x + \frac{2\pi g}{d_x} \right)^2 - k_y^2} \right), \quad (3)$$

where $\varepsilon_{\mathrm{sub}}$ is the substrate dielectric constant.

The method allows us to calculate, via the full scattering matrix of the system $\mathbb{S}$, all $4N_G$ (where $N_G = 2G+1$) amplitudes of the full set of outgoing harmonics [Eqs. (2) and (3)], if the amplitudes of all $4N_G$ incoming Bragg harmonics $\mathbf{k}_g^{\mathrm{in,vac}} = (k_{g,x}, k_y, k_{g,z}^{\mathrm{vac}})$ and $\mathbf{k}_g^{\mathrm{in,sub}} = (k_{g,x}, k_y, -k_{g,z}^{\mathrm{sub}})$ are known.

In the limit $G \to \infty$, the $\mathbb{S}$-matrix represents the asymptotically exact solution of Maxwell's equations for the PCS. In the numerical calculations, however, we truncate $\mathbb{S}$ at some finite $4N_G \times 4N_G$ matrix. The scattering matrix is used instead of the more familiar transfer matrix formalism, in order to avoid the otherwise inevitable numerical instabilities due to evanescent waves for higher reciprocal lattice vectors.

The method allows to calculate the frequency dependencies of the reflectivity, transmissivity, diffraction and absorption coefficients, and also the spatial distribution of the electromagnetic fields inside the structure.

The input parameters of the method are the geometrical sizes of the structure and the dielectric susceptibilities of the constituent materials. The latter are treated as spatially local and frequency dependent, which is especially important in case of metals. The dielectric function of gold was taken from Ref. 31. The ITO dielectric susceptibility dispersion was taken into account as well; see Ref. 15.

The convergence of the truncated scattering matrix with N_G is an important problem in case of metals and depends, as is well known, on the polarization of the incoming light. If the light is polarized along the wires (TE polarization), calculations of the transmission spectra with $N_G = 49$ provide an estimated relative error smaller than 0.01%. The convergence in TM polarization (electric field components perpendicular to the wires) is much slower, although we have employed the idea of Ref. 32, thus significantly improving the convergence. The TM spectra were usually calculated with $N_G = 301$, and several checks with N_G up to 1000 allow us to estimate the relative error as $\approx 1\%$. The real problem here is that the computing time of this method is proportional to N_G^3, which means that, with the increase of the number of harmonics used, it quickly becomes impractical even on a supercomputer.

The physical reason for the slow convergence of the Fourier-series-based methods in the case of PCS with nanostructured metals is the very strong change of the electric field near the metal surface, especially if the latter has sharp features. However, a comparison of our calculations with experimental results shows that this method produces a very good qualitative agreement with the measured results in all cases, without using additional fitting parameters. In Sec. IV, a slightly smaller gold nanowire thickness was used in the calculations if compared with the experimental value in order to obtain a better agreement with the measured nanowire plasmon energy. We especially emphasize all cases of such differences which are most likely due to uncertainties in the experimentally measured dimensions or the dielectric susceptibilities.

IV. RAYLEIGH ANOMALIES IN METALLO-DIELECTRIC NANOSTRUCTURES

We start from the investigation of systems with a thinner ITO layer, not supporting any guided modes in the spectral range of the nanowire plasmon resonances. As already mentioned, the optical response of a periodic arrangement of metallic scatterers can differ substantially from that of noninteracting individual metallic particles. It turns out that the period of the grating structure is the crucial parameter for the modification of the isolated nanowire plasmon response. This can be interpreted as a manifestation of the nanowire-nanowire interaction in the far-field regime.

In Fig. 2, a collection of measured [(a),(c)] and calculated [(b),(d)] extinction [$-\ln(T)$, T: transmission] spectra for gold nanowire arrays on top of a 15-nm-thick ITO layer are depicted. Panels (a) and (b) contain period-dependent spectra recorded at normal incidence ($\varphi = \vartheta = 0°$). From top to bottom, the grating period d_x is increased from 350 nm to 500 nm in steps of 50 nm. In panels (c) and (d), an overview of the angular dependence for a fixed nanowire period of $d_x = 450$ nm is given. The azimuthal angle $\varphi = 0°$ remains unchanged, and the polar angle ϑ is varied between 0° and 18° in steps of 6°. Beside the more relevant case of TM-polarization (the magnetic field parallel to the nanowires), also the corresponding spectra for TE-polarization (electric field parallel to the nanowires) are displayed. All extinction spectra exhibit pronounced spectral features with distinct dependencies on the grating period as well as on the angle of incidence.

Note that, instead of the assumed 20 nm (experiment), all calculations of Sec. IV were performed for gold nanowires with a height of 15 nm, while the wire width of 100 nm has been retained unchanged. This minor modification, causing a red shift of the calculated nanowire plasmon peak, leads to a better quantitative agreement between experiment and theory. Otherwise, assuming the height of 20 nm, the calculated nanowire plasmon peak energy is about 100 meV

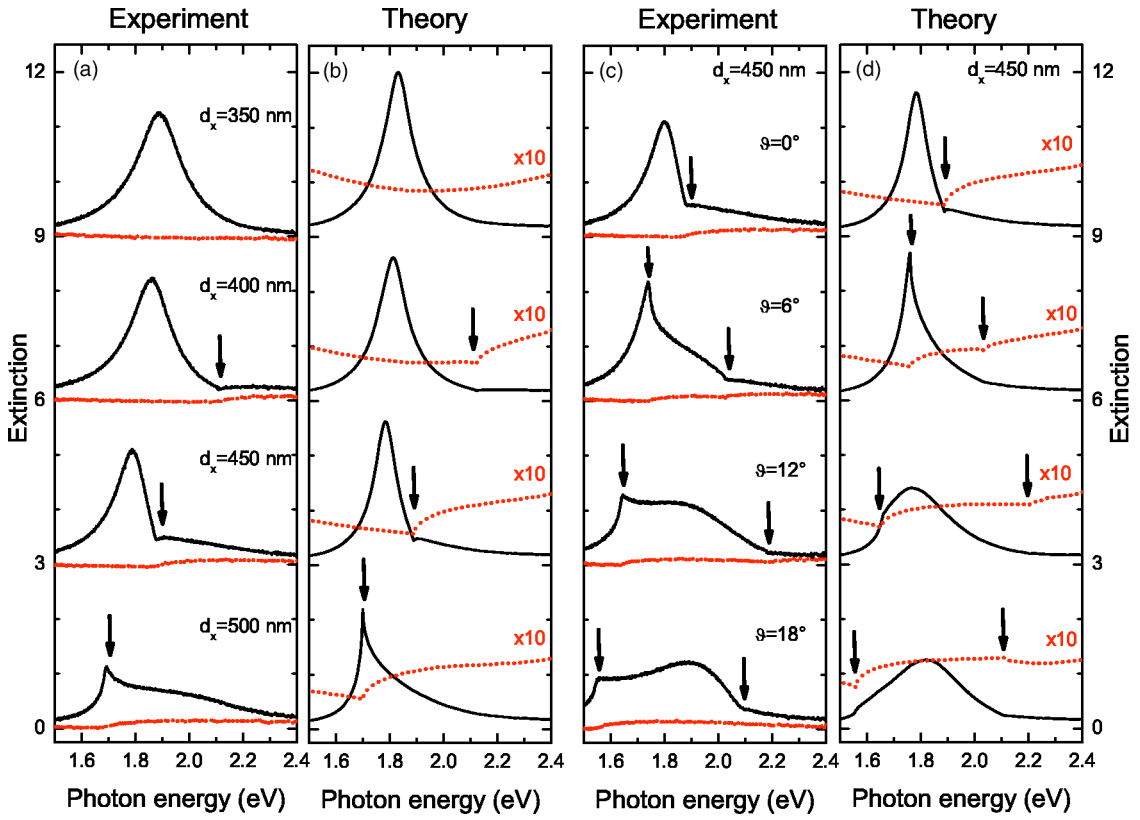

FIG. 2. A collection of measured (a) and calculated (b) extinction spectra for nanowire gratings on top of 15-nm-thick ITO layers at normal incidence. From top to bottom, the nanowire period d_x is changed from 350 nm to 500 nm in steps of 50 nm. In addition, measured (c) and calculated (d) extinction spectra for different angles of incidence and a fixed nanowire period of 450 nm are depicted. Spectra are shown for TE- (dotted lines) and TM-polarization (solid lines) (electric and magnetic field parallel to the nanowires, respectively). TE-polarized spectra in (b) and (d) are drawn to a larger scale (x10). The individual spectra are shifted upwards for clarity in each panel. Vertical arrows mark the positions of the diffractive anomalies.

higher than that seen experimentally. This deviation can be due to uncertainties in the exact experimental determination of the nanowire geometry or the ITO dielectric function.

A detailed analysis of the displayed period-dependent results [Figs. 2(a) and 2(b)] shows that the undisturbed plasmon resonance of the quasi noninteracting nanowires can only be seen for a period of d_x=350 nm and TM-polarization (oscillation of the conduction band electrons of the metal nanowires perpendicular to the nanowire axis). Neither near- nor far-field effects influence the isolated broad resonance, centered at approximately 1.9 eV, which can be attributed to the excitation of the particle plasmons of the individual gold nanowires. The spectral shape of this strong plasmon resonance is clearly modified by increasing the nanowire period. As indicated by the arrows, an additional cusp-like anomaly occurs for nanowire periods exceeding d_x=350 nm. With increasing d_x this anomaly shifts to lower energies.

The variation of the angle of incidence for a fixed nanowire period shows strong spectral modifications, too. In Figs. 2(c) and 2(d), the anomaly splits for oblique incidence, and two dips or kinks, shifting in opposite directions with increasing ϑ, become visible. It is important to notice that all anomalies show up at an identical spectral position for TE- and TM-polarizations, although they are less pronounced for TE-polarization (see the dotted lines).

Rayleigh-type anomalies have to be considered as the physical origin of the spectral features reported here. The Rayleigh anomalies are due to the opening of new diffraction orders. Or, more precisely, they appear when the light field of some Bragg harmonics [see Eqs. (2) and (3)] changes from evanescent to radiative in ambient air or substrate layers at a given frequency. This happens when the term under the square root in Eqs. (2) and (3) changes the sign from negative to positive,

$$\omega_{\text{Rayleigh}} = \frac{c}{\sqrt{\varepsilon}}\sqrt{k_{g,x}^2 + k_y^2}, \tag{4}$$

where $\varepsilon=\varepsilon_{\text{sub}}=2.14$ for the quartz substrate or $\varepsilon=\varepsilon_{\text{vac}}=1$ for air ambience. Since these anomalies are connected with the asymptotic far-field behavior (radiating conditions), they depend only on the dielectric constants of the substrate and the ambient layer. In agreement with the experiment, there is no dependence on the near-field and, thus, on the polarization state of the incoming light or the dielectric susceptibilities of the PCS itself. We have to mention that several recent publications which refer to dipolar particle interaction have already addressed similar optical phenomena of periodic gold nanostructures.[23,33,34] Although no sharp spectral features were found in these measurements (presumably due to poor

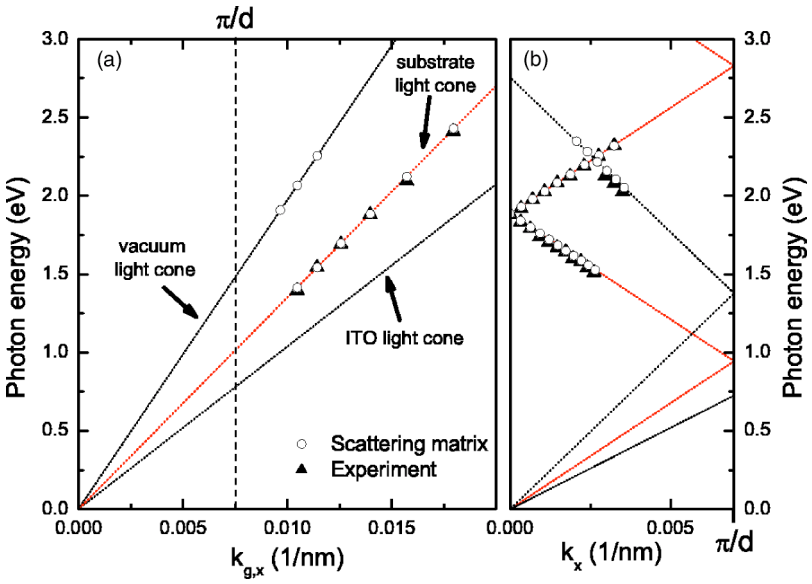

FIG. 3. Measured and calculated spectral positions of the observed grating anomalies. The dependency on the grating period (normal incidence: $k_{g,x}=2\pi/d_x$) is shown in panel (a). A period of $d_x=450$ nm was chosen for the angle resolved experiments (variation of k_x) in panel (b). Light cones for air, quartz, and ITO are depicted as dotted lines. Additionally, the dispersion of the light cones folded into the first BZ are displayed in panel (b).

angular resolution in the measurement setup), it has already been shown that scattering effects can lead to strong modifications of the particle plasmon resonance.

For an exact interpretation of the spectra displayed in Fig. 2, the peak positions of all spectral features have been determined for the whole sample series. Figure 3 shows the period- and angle-dependent dispersions of the measured anomalies, in comparison with the light cones of the air environment and the quartz substrate. At normal incidence where $\vartheta=\varphi=0°$ with $k_x=0$, following Eq. (4), the dependence of the anomalies on $k_{g,x}=2\pi/d_x$ can be probed by changing the nanowire grating period, as displayed in panel (a). The dependence on $k_x=k_0 \sin\vartheta$ is depicted in panel (b), extracted from angle of incidence dependent measurements at a fixed period of $d_x=450$ nm. The light cones of air and quartz, folded into the 1st Brillouin zone (BZ) in (b), are shown as lines in both panels. As anticipated, all the measured (and calculated) anomalies lie exactly on these light cones. Based on these excellent polarization-independent fits, the interpretation as Rayleigh anomalies is appropriate. Note that the Rayleigh anomalies are weak when detuned far from the particle plasmon resonance. They become resonantly increased when approaching the nanowire plasmon extinction peak. Note also an inversion of the cusp-like Rayleigh anomaly while crossing the isolated nanowire plasmon band (see Fig. 2).

Another important experimental confirmation is the direct observation of the Bragg-diffracted light field components in *x*-direction. Dependent on the grating period, they appear as visible bright spots at the edges of the quartz substrate during our measurements (not shown here).

To support our conclusion further, we have performed additional calculations for a free-standing structure without any quartz substrate below the ITO layers. Such structures have not been realized experimentally, but they present an instructive model. The ITO layer thickness is taken as 15 nm, and the gold nanowire cross section (100×15 nm^2) has been retained unchanged. The calculated extinction spectra are shown in Fig. 4(a). For a direct comparison, the same calculations for an identical structure with a quartz substrate below the 15-nm-thick ITO are additionally depicted in panel (b) (the same calculations as in Fig. 2). From top to bottom, the nanowire period is increased from 150 nm to 800 nm in steps of 50 nm in both panels. In comparison with the free-standing structures, all spectra of panel (b) are slightly shifted to lower energies due to the changed dielectric surroundings of the gold nanowires. Although identical periods have been assumed for the calculation of both structures, the sharp spectral features visible in panel (b) for nanowire periods ranging from 350 nm to 500 nm disappear for the spectra in panel (a). Due to the missing quartz substrate, the substrate-induced Rayleigh anomalies are absent. Only for $d_x\approx650$ nm, the far-field interaction phenomena can be seen for both structures, connected with the vacuum-induced Rayleigh anomaly (cusp-like structure). In contrast to the pure Rayleigh-type anomalies in panel (b), the narrow structures in Fig. 4(a) for periods of $d_x=550$, 600, and 700 nm are actually resonance anomalies. The inset of Fig. 4(a) clearly demonstrates the Fano-type nature of these sharp resonances. They appear due to the excitation of quasiguided modes in this free-standing structure (see the discussion in Section V for more details).

To conclude, the presented results show clearly that the observed interaction phenomena rely on a collective scattering effect of the whole nanowire ensemble. In contrast to near-field phenomena ($d_x<300$ nm), which are based on the nanowire-nanowire interaction via evanescent fields, such grating effects only appear for nanowire samples with larger periods ($d_x>350$ nm). For this special regime, the optical near-fields (acting on the individual metal nanowires) are strongly modified due to the opening of new diffraction orders. As a result, the characteristic nanowire far-field distribution and therefore the shape of the nanowire plasmon resonances are changed, as has been shown in Fig. 2.

Although the discussion of near-field coupling phenomena at smaller periods exceeds the scope of the current work, we have to mention that the calculated spectra in Figs. 4(a) and 4(b) give clear evidence for them. The enhanced near-

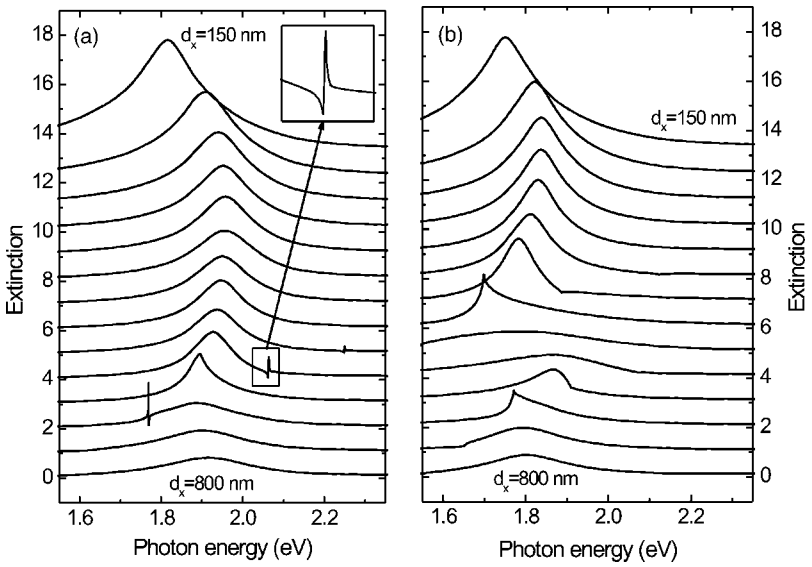

FIG. 4. Calculated spectra (TM-polarization, normal incidence) for gold nanowire gratings on top of a free-standing 15-nm-thick ITO film are shown in panel (a). Panel (b) displays the calculated spectra for an identical structure, but without removing the quartz substrate below the ITO layer (the same structure as assumed for the calculations in Fig. 2). From top to bottom, the nanowire period d_x is changed from 150 nm to 800 nm in steps of 50 nm. The individual spectra are shifted upwards for clarity. Inset: Fano-type resonance for a nanowire period of 600 nm.

field coupling for a decreased nanowire period $d_x < 300$ nm) induces a red shift and broadening of the nanowire plasmon resonances. Similar effects have already been demonstrated for two-dimensional gold nanoparticle arrays.[21] These near-field coupling phenomena can be explained by the dipole-dipole interaction between the individual gold nanowires and have to show a $(a/d_x)^{-2}$ dependence (a is the nanowire width).

V. POLARITONIC PHOTONIC CRYSTAL SLAB

In Sec. IV, we have shown that the observed far-field interaction phenomena for gold nanowire gratings deposited on top of 15-nm-thick ITO layers are based on a collective substrate-induced scattering effect at the Rayleigh wavelength. In addition to these results, we will now discuss another interaction effect due to waveguiding anomalies (resonant anomalies) of thicker ITO layers. We will show that the optical properties of similar gold grating structures on top of 140-nm-thick ITO layers are primarily dominated by an additional strong coupling phenomenon. In particular, we will give evidence that the interaction of electronic and photonic resonances of metallic photonic crystal slabs can lead to the formation of a waveguide-plasmon polariton.[15]

A. Empty-lattice approximation

In contrast to a 15-nm-thick ITO layer, a 140-nm-thick ITO slab deposited on a quartz substrate supports guided modes in the spectral range of the considered nanowire plasmon resonances. Therefore the metallic photonic crystal slab provides electronic and optical resonances simultaneously. The resulting spectral modifications can be clearly observed. For example, Fig. 5 shows the measured spectra of gold nanowire arrays with an identical period of $d_x = 450$ nm with 15 (a) and 140-nm-thick (b) ITO layers. The shape of the nanowire plasmon resonance for samples with a thicker guiding ITO layer differs substantially from that discussed previously. The spectra for TE- and TM-polarization in panel (b) are now characterized by an additional extinction maximum. We will show that this maximum arises due to the interaction with the lowest TE or TM guided modes. Here, the strongly asymmetric shape of the resonances can be attributed to the Fano-type nature of the excited waveguide resonance. Although diffractive Rayleigh anomalies can still be seen for such structures, waveguiding anomalies dominate the spectral response of the interacting waveguide-nanowire-system.

To understand the energy dispersions of the different resonances in the modified structure, we start from a simple empty-lattice approximation. As a first step of this approximation for a metallic grating-waveguide structure, we replace it by a homogeneous ITO layer. The energy dispersions of the lowest transverse electric (TE_0) and transverse mag-

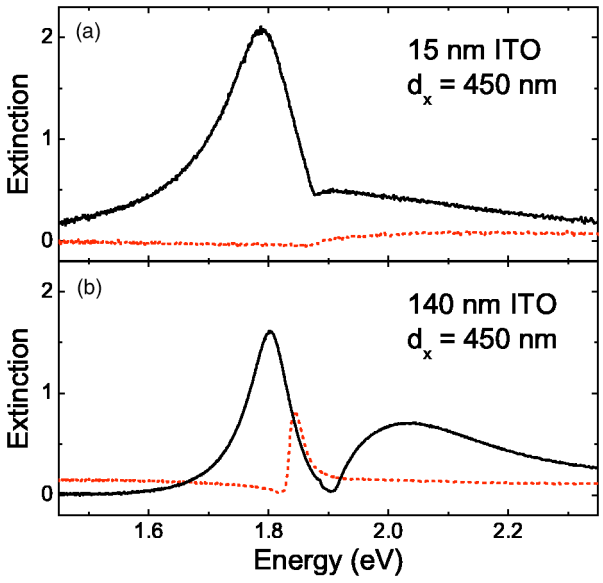

FIG. 5. Measured extinction spectra of gold nanowire arrays (Period $d_x = 450$ nm) for normal light incidence. Spectra of samples with 15-nm-thick (a) and 140-nm-thick (b) ITO layers are shown for a comparison in TE (dotted lines) and TM (solid lines) polarization.

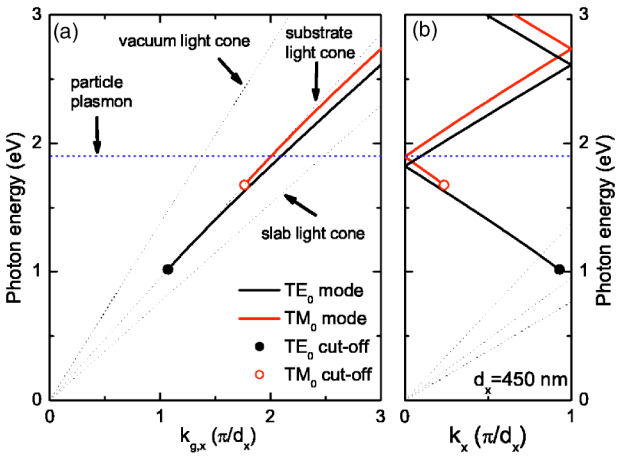

FIG. 6. Empty-lattice approximation: The lowest TE and TM polarized guided modes of a homogeneous and 140-nm-thick ITO waveguide. Their dependencies on $k_{g,x}$ are shown in panel (a). Panel (b) displays these guided modes folded into the first BZ for an assumed grating period of d_x=450 nm. The particle plasmon dispersion of noninteracting gold nanowires (dotted horizontal line) is shown too.

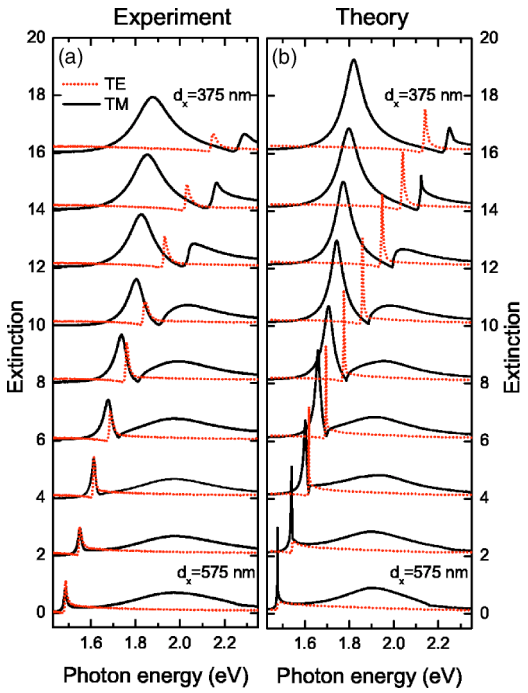

FIG. 7. Measured (a) and calculated (b) extinction spectra of gold nanowire arrays deposited on top of 140-nm-thick ITO layers for normal light incidence and nanowire periods ranging from 375 nm to 575 nm in steps of 25 nm. Spectra for TE (dotted line) and TM (solid line) polarization are shown. The individual spectra are shifted upwards for clarity in each panel.

netic (TM_0) guided modes can then be found from the solution of the transcendent equations for the waveguide slab (see, e.g., in Ref. 35).

When assuming a surface corrugation with periodicity d_x in a second step, we have to fold back the guided modes into the first Brillouin zone of the 1D photonic crystal slab. These folded (due to the periodic surface corrugation) modes are now located above the air light cone and can couple to the photon continua of the air environment and the quartz substrate. Therefore, the formerly guided modes of the uncorrugated structure become leaky (quasiguided). Such modes are characterized by relatively long lifetimes and large quality factors and may lead to resonantly enhanced fields inside the planar photonic crystal structures. As a result, the dispersion of these quasiguided modes can be probed by period- and angular-dependent transmission measurements, where they will show up as sharp spectral resonances in the transmission or extinction (see, e.g., in Ref. 28 and references therein).

The results of this empty-lattice approximation are shown in Fig. 6 for a sample structure with an ITO layer thickness of L_z=140 nm. Panel (a) displays the lowest TE_0 and TM_0 guided modes of the homogeneous ITO waveguide on top of a quartz substrate. For simplicity, we neglect the frequency dispersion of the ITO dielectric susceptibility in this qualitative discussion and assume ε_{ITO}=3.61. It is important that in the asymmetric guiding structure on the quartz substrate, TE_0 and TM_0 modes do not exist for energies below their cut-off frequencies. For example, structures with a 15-nm-thick ITO layer on top of a quartz substrate do not support quasiguided modes in the visible part of the spectrum, because their cut-off is shifted to much higher energies. The folded guided modes, as explained above, are displayed in panel (b) for an assumed grating period of d_x=450 nm. Note that for the degenerate Bragg resonances in the center and borders of the first BZ, the degeneracy is lifted if the neglected corrugation is taken into account.

Up to now we did not consider the metallic properties of the corrugated structure. If we neglect the electromagnetic coupling between the individual metal nanowires, the resulting flat dispersion of the nanowire particle plasmon can be depicted as a horizontal line at approximately 1.9 eV (the dotted line in Fig. 6).

For an assumed period of d_x=450 nm and TM polarization, especially the band located at 1.9 eV in the center of the first BZ is quite important [see Fig. 6(b)]. It is a degenerate triplet in this simple noninteracting picture, originating from the Bragg resonance of the lowest TM_0 guided modes with $k_{g,x}=\pm 2\pi/d_x$ and the uncoupled nanowire plasmon resonance.

According to the observations in Fig. 5(b), where two resonances have been detected for TM polarization at normal incidence, this degenerated triplet is actually split off. The reason for that is the periodic corrugation and the strong coupling between the electronic and optical modes. Similar interaction phenomena have already been discussed for excitonic systems.[8,36] We will consider this behavior in Sec. V B.

B. Waveguide-plasmon polaritons

The experimental and theoretical verification of strong coupling in metallic photonic crystals is depicted in Fig. 7. In this figure, the measured and calculated extinction spectra of gold nanowire arrays deposited on top of 140-nm-thick ITO layers are shown for normal light incidence and different grating periods d_x. Here, we have assumed a nanowire width

of 100 nm and a nanowire height of 20 nm for the scattering-matrix based calculations. For TE polarization, only one sharp spectral feature appears in each spectrum, because no nanowire plasmons can be excited for this special polarization. The existing narrow peaks can be related to the excitation of TE quasiguided modes, which are characteristic features of waveguiding photonic crystal structures. Thus, these spectrally asymmetrically shaped Fano-type resonances are not found in spectra for thinner ITO layers which do not support quasiguided modes for this spectral range. In our measurement geometry, these spectral features arise due to the grating-induced Bragg resonance of the TE_0 waveguide modes with $k_{x,g}=\pm 2\pi/d_x$. The figure clearly demonstrates that a change of the Bragg condition, caused by increasing the grating period d_x shifts the TE_0 quasiguided mode to lower energies. In principle, as already discussed earlier in this chapter, two quasiguided modes should exist at normal incidence, leading to a small stopband at the center of the first BZ. However, due to the mirror symmetry of the structure, only the upper symmetric quasiguided mode can be excited at normal incidence.[37] As is common for such structures, the lower antisymmetric mode is optically inactive and can only be observed for transmission measurements under inclined incidence.

Again, our attention has to be focused on the more significant case of TM polarization. In contrast to TE polarization, all TM polarized spectra of Fig. 7 exhibit two extinction maxima. For example, the extinction spectra for a period of $d_x=575$ nm are characterized by a narrow peak at 1.5 eV and an additional broader peak centered at 2 eV. The broader peak can be attributed to the particle plasmon of the individual gold nanowires. Like in TE polarization, the narrower extinction resonance is due to the excitation of the TM_0 quasiguided mode. Reducing the nanowire period shifts the TM_0 quasiguided mode spectrally closer to the nanowire plasmon resonance. Due to strong coupling between the waveguide and nanowire plasmon resonances, we observe a strong anticrossing of the modes instead of their spectral overlap. This situation is comparable to the normal mode coupling in semiconductor microcavities,[38] where the splitting can be interpreted as the formation of a new polaritonic state. The dispersions of the polariton branches are depicted in Fig. 8, nicely demonstrating the strong coupling phenomena. In this figure, the maxima extracted from all measured and calculated extinction spectra are plotted for comparison. Besides the excellent agreement between the experimental and calculated values, especially the large Rabi splitting of 250 meV between the upper and lower polariton branches is very conspicuous.

The strong coupling effects lead to a more dramatic modification of the interacting systems compared to the diffractive interaction phenomena of gold nanowire structures on thin ITO layers. The key for understanding this spectacular behavior is to realize that we no longer investigate the properties of an individual metal nanowire, but rather the extinction of a new compound system, namely a strongly coupled *waveguide-plasmon polariton* system. As already discussed in our previous publication,[15] the anticrossing behavior and thus the formation of a new polariton can be easily modeled in a simple resonance approximation, accounting for coupling between the isolated wire plasmon and a pair of counter-propagating guided TM_0 modes with momenta $k_x \pm 2\pi/d_x$.

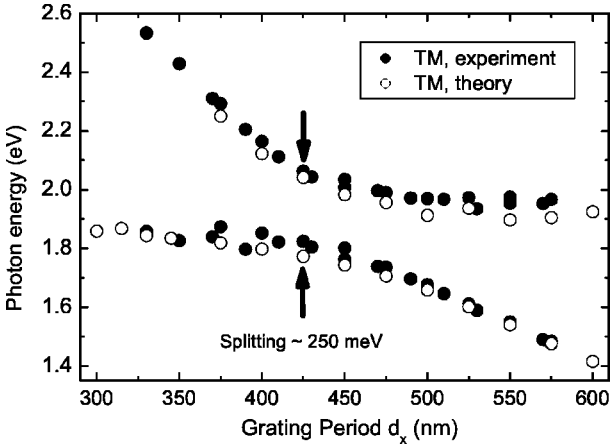

FIG. 8. Measured (hollow circles) and calculated (solid circles) energies of the extinction spectra maxima for gold nanowire arrays deposited on top of 140-nm-thick ITO layers. The dependence on d_x for normal light incidence and TM polarization is shown.

Returning to the model calculations for the free-standing nanowire structure on top of a 15-nm-thick ITO layer with removed quartz substrate [see Fig. 4(a)], we now can further improve the analysis of the sharp spectral features for nanowire periods of $d_x=550$ nm, 600 nm, and 700 nm. Although we assume a very thin (only 15-nm-thick) ITO substrate in these calculations, this symmetric structure supports quasiguided modes. The frequency cut-offs for TE_0 and TM_0 modes are zero for any guiding layer thickness in case of symmetric waveguide structures (the same materials below and above the waveguide). Thus, when removing the substrate, the TM_0 mode exists in our symmetric 15-nm-thick ITO structure as well. These spectrally narrow resonances cannot be found for identical structures with an additional quartz substrate, as can be seen in the calculations for the asymmetric structures [see Fig. 4(b)]. Here, instead of sharp resonances, only the cusp-like Rayleigh anomalies are visible. It is important to remark that the small thickness of the ITO waveguide has a large influence on the observed coupling phenomena in the case of symmetric structures. As a consequence of the ITO thickness, the energy distance between the TM_0 mode and the vacuum light cone is very small, $\sim$3 meV only. Additionally, the integrated polarization of the TM_0 guided mode is reduced, and, as a result, its coupling with the plasmon resonance is relatively weak. The first point explains the existence of the waveguiding anomalies in TM polarization in Fig. 4 notwithstanding the small ITO thickness. The second point explains why the Rayleigh anomalies are not seen: they are very close to the waveguiding anomalies. And the third point explains the apparent absence of the waveguide-plasmon anticrossing effect: actually, we deal with the weak coupling regime here. Only at $d_x=650$ nm the cusp-like anomaly (exactly on the vacuum light cone) dominates the spectra in the vicinity of the nanowire plasmon, and the waveguide anomaly does not show up at all. This is explained by a plasmon resonant enhancement of

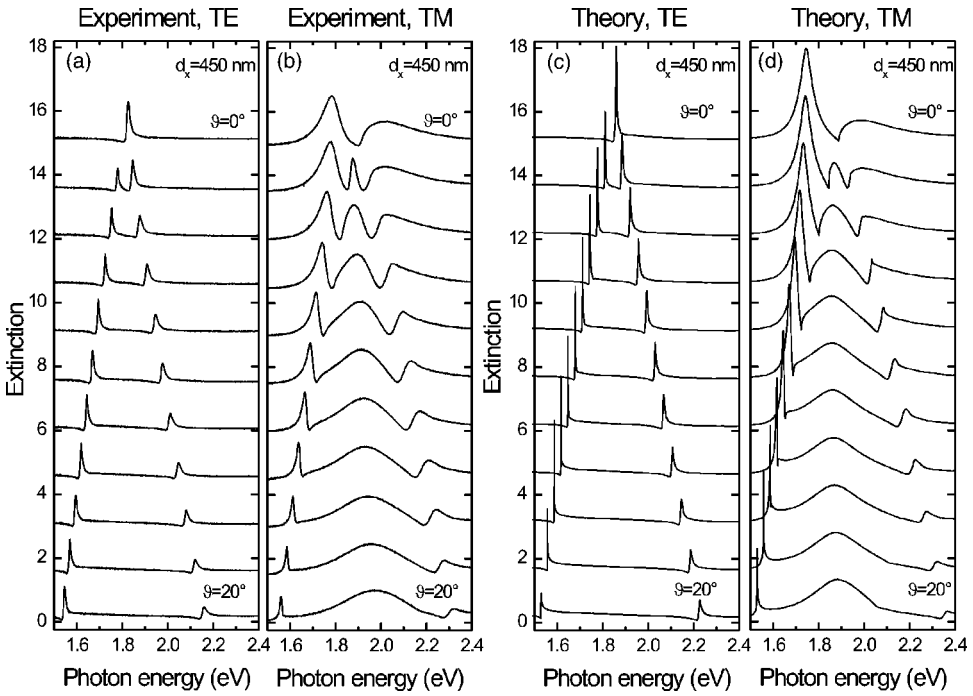

FIG. 9. Measured (a),(b) and calculated (c),(d) extinction spectra of gold nanowire arrays deposited on top of 140-nm-thick ITO layers for a fixed nanowire period of d_x=450 nm. From top to bottom, the angle ϑ is increased from 0° to 20° in steps of 2° while φ=0° remains unchanged. Spectra for TE (a),(c) and TM (b),(d) polarization are depicted. The different spectra are shifted upwards for clarity in each panel.

the Rayleigh anomaly. We plan to discuss this behavior in more detail elsewhere.

C. Dispersion properties

The dispersion properties of the different resonances have been measured via transmission experiments by changing the angles of incidence ϑ and φ. Only two cases of azimuthal angle, φ=0° and 90°, will be discussed. In these cases the plane of incidence is orientated either perpendicular or along the nanowires, respectively. The results of the first set of measurements on a gold nanowire sample with fixed period d_x=450 nm are displayed in Fig. 9 for TE (a) and TM (b) polarization. For these transmission measurements, the angle ϑ was increased from 0° to 20° in steps of 2° while φ=0° remained unchanged. Additionally, the theoretically obtained spectra are shown in Fig. 9 for TE (c) and TM (d) polarization. We have again assumed gold nanowires with a width of 100 nm and a height of 20 nm on top of a 140-nm-thick ITO layer for these calculations. It is clearly visible that the single resonance at normal incidence splits up for inclined incidence in TE polarization (a),(c). The narrow peaks are due to the excitation of quasiguided TE modes of the PCS with momenta $k_{g,x}=k_x\pm 2\pi/d_x$. Now the formerly not visible antisymmetric TE mode can be excited in transmission measurements for angles of incidence $\vartheta\neq 0°$. Also in TM polarization (b),(d) an additional peak appears between the two polariton branches for inclined incidence with $\vartheta\neq 0°$. With the change of ϑ, the plasmon resonance exhibits an anticrossing behavior with the narrower symmetric and antisymmetric TM polarized waveguide modes. All experimental results are reproduced by our calculations with excellent qualitative correspondence.

The energy positions of the measured and calculated extinction maxima are shown in Fig. 10 as solid and open symbols. We will show in the next section that the near-field is enhanced at the energies of such extinction maxima. In other words, the extinction maxima correspond to the energy positions of the resonant in-plane excitations of the PCS. It is interesting that in the resonant structure with d_x=450 nm, the stopbands of these excitations in TE and TM polarization

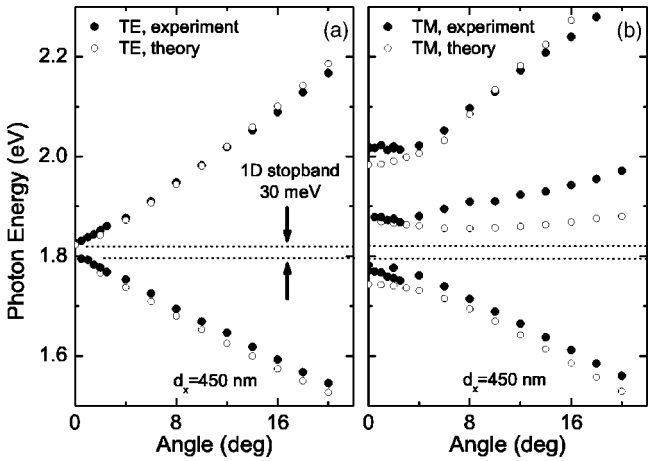

FIG. 10. Measured (solid circles) and calculated (open circles) positions of the extinction spectra maxima in TE and TM polarization for nanowire arrays on top of 140-nm-thick ITO layers. The angle ϑ is increased from 0° to 20° while φ=0° and d_x=450 nm remain unchanged. The arrows show the 1D stopbands in TE and TM polarizations.

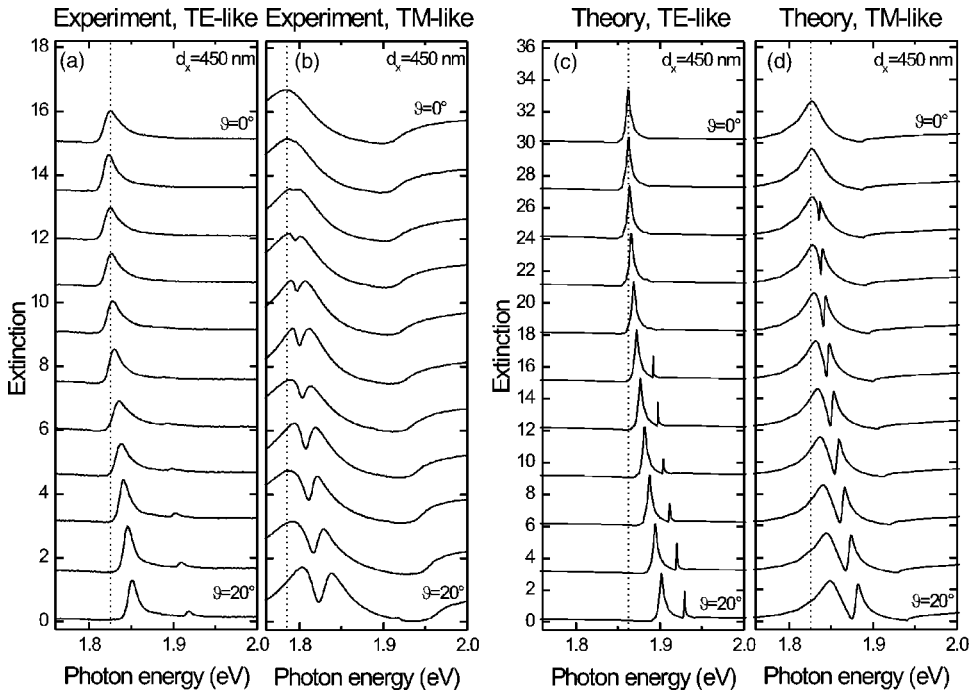

FIG. 11. Measured (a),(b) and calculated (c),(d) extinction spectra of gold nanowire arrays deposited on top of 140-nm-thick ITO layers for a fixed nanowire period of d_x=450 nm. From top to bottom the angle ϑ is increased from 0 to 20° in steps of 2° while φ=90° remains unchanged. Spectra for TE-like (a),(c) and TM-like (b),(d) polarization are depicted. For the calculations a wire cross-section of 85 $\times$30 nm^2 has been assumed to bring the calculated wire plasmon resonance to better agreement with the measured one. The individual spectra are shifted upwards for clarity in each panel.

overlap. Therefore, the structure reveals a full (i.e., for all polarizations) 1D stopband for transmission in the *x*-direction.

In addition, we have performed similar measurements and calculations for another fixed azimuthal angle, φ=90°. The polar angle ϑ was again increased from 0° to 20° in steps of 2°. Thus, the plane of light incidence is perpendicular to the slab plane, as before, but now parallel to the wires. In this geometry, the electric field is oriented perpendicular to the wires in case of *s*-polarization. Thus, *s*-polarization becomes TM-like, and a coupling with the wire plasmon is anticipated. For *p*-polarization, the electric field has components along the nanowires, and perpendicular to the nanowires along the *z*-direction. This means that no particle plasmon resonances of the gold nanowires exist in the range of light frequencies investigated in the latter case.

In Fig. 11, the measured and calculated spectra for *p*-polarized (a),(c) and *s*-polarized (b),(d) light are depicted for different angles of incidence. From top to bottom, the angle ϑ is increased from 0° to 20° in steps of 2° while φ =90° remains unchanged. Again, the theory reproduces the measured behavior quite well. We have to mention that the theoretically assumed nanowire dimensions have been modified slightly. The observed phenomena depend critically on the nanowire plasmon position. Therefore, we employed a wire cross-section of 85$\times$30 nm^2 in our calculations to get a better qualitative agreement with the experimentally measured spectra. As anticipated, the strong extinction peaks seen at normal incidence remain the dominant features at ϑ $\neq$0°, too. However, a new narrow mode becomes visible for each polarization with the increase of ϑ at fixed φ=90°. Note that, according to Eq. (1), this geometry corresponds to the incoming light momentum $\mathbf{k}=(0, k_0 \sin\vartheta, k_0 \cos\vartheta)$. Thus, increasing the angle of incidence in this geometry, we actually measure the dispersion of the resonant modes along the nanowires.

In order to identify the additional modes, it is instructive to compare the calculated spectra (at ϑ=20°) between a symmetric situation (plane of incidence along the wires, φ =90°) and a slightly distorted case with φ=88°. The results of such a calculation are shown in Fig. 12 for TE-like and TM-like polarization simultaneously. Important information can be deduced by comparing the spectra of panel (a) and panel (b). Additional modes become visible at φ=88°, because this situation corresponds to a small k_x $=k_0 \sin\vartheta \sin 2° \approx 0.035 k_y$. The strongest extinction peak in *p*-polarization near the Γ-point is the symmetric TE$_s$ mode, following the analysis above. The extra mode appearing at $k_x \neq 0$ in *p*-polarization at lower energies is the antisymmetric (in Γ) counterpart TE$_a$, as we already know. Because this mode coincides exactly with the extra mode seen in the *s*-polarization at φ=88° (see the arrows in Fig. 12), we can attribute this extra mode to the TE$_a$ one. Thus, the incoming *s*-polarized light (predominantly TM-like) can excite the TE$_a$ mode in this geometry. The physical reason for coupling of TM- and TE-like modes is the following. Although for ϑ $\neq$0° and $\varphi \neq$0° the main harmonics is propagating along the wires (k_x=0, $k_y \neq 0$), the higher Bragg harmonics are inclined, $k_{g,x} \neq 0$, $k_y \neq 0$, and therefore provide the observed polarization coupling.

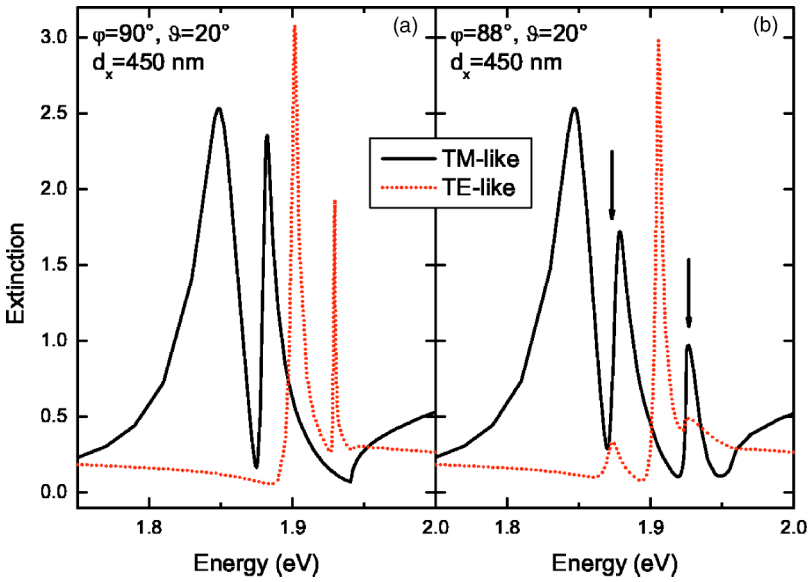

FIG. 12. Calculated extinction spectra for a fixed nanowire period of $d_x=450$ nm and a fixed angle of $\vartheta=20°$. Calculations for $\varphi=90°$ [panel (a)] and $\varphi=88°$ [panel (b)] are compared. Spectra for TE-like (dotted lines, *p*-polarization) and TM-like polarization (solid lines, *s*-polarization) are depicted. Again, a wire cross-section of 85 $\times 30$ nm^2 has been assumed. The arrows in (b) correspond to the spectral positions of the extra modes.

Repeating the same procedure with the extra mode appearing in *p*-polarization (predominantly TE-like), we see that the extra mode is of the TM_a type, i.e., becomes antisymmetric at the Γ-point.

It is interesting that this coupling with modes in another polarization is resonantly increased near the wire plasmon resonance. Therefore the additional modes are very weak for larger or smaller periods of d_x, although the extra modes are nominally present in the measured and calculated spectra.

The blue shift of all the modes with the increase of ϑ (that is, of k_y) is apparently quadratic in k_y due to the free light propagation in the *y* direction (with no modulation), as anticipated.

D. Electromagnetic near-field distribution

In order to extend the spectral analysis of Sec. V B and to investigate the underlying strong coupling phenomena in greater detail, it is very instructive to take a closer look at the near-field distribution of the coupled nanowire-waveguide system. The knowledge of such near-field distributions is not only important for understanding the physical mechanisms of the observed coupling phenomena, but can also help to control the nonlinear optical response in possible future applications. In this section, we restrict ourselves to the discussion of the calculated near-field distribution, although experimental measurements with a scanning near-field microscope should be possible at least near the sample surface.[39] All calculations which we are going to present are done within the scattering-matrix formalism. Because of very good qualitative agreement down to minor details between all calculated and measured extinction spectra, we assume that the calculations of the electromagnetic field distributions give a qualitatively correct picture. All deduced informations support our previous conclusions exactly.

To understand the main features of the complex near-field distributions, we will limit our discussion to structures with a period of $d_x=450$ nm, TM-polarization, and normal light incidence ($\vartheta=\varphi=0°$). Additionally, the field distributions are only shown for two characteristic photon energies at the waveguide-plasmon resonance. Figures 13 and 14 display the field distributions at the position of the lower polariton branch and at the extinction minimum between the two polariton branches. Due to a small spectral shift between theoretical and experimental results, the corresponding energies have to be assumed as 1.74 eV for the extinction maximum of the lower polariton branch (see Fig. 13) and 1.9 eV for the extinction minimum between the two polariton branches (see Fig. 14) in our theoretical considerations. The electric (a),(b) and magnetic (c),(d) field vectors are shown as a two-dimensional array of colored cones (online) in the figures. The length of the cones is proportional to the field strength at the central point of each cone, and they specify the respective field direction by their orientation. However, such vector distributions are oscillating with time and cannot be displayed in a static picture. Thus, we are showing the near-field distributions at the most characteristic moments of time, when the integrated intensity of the corresponding fields reaches its maximum value (see below).

Like in the beginning of this section, we again assume 100-nm-wide and 20-nm-thick gold nanowires on top of a 140-nm-thick ITO waveguide. The schematic cross-section of the PCS is displayed by solid lines (magenta online) in each figure. In panels (a) and (c), the positions of the gold nanowires are indicated by rectangular regions above the 140-nm-thick ITO layer. In addition, the field distributions near the gold nanowires are drawn to a larger scale in panels (b) and (d). Note that the incoming light field propagates from the top ($z<0$) to the bottom ($z>0$) of the figure in all calculations.

To understand the basis of the coupling phenomena, all fields are depicted in Figs. 13 and 14 at the moments of time when the intensity of the corresponding field averaged over the displayed cross-section reaches a maximum. Additional important information is provided by the calculated quantities t/T, η, and $E_{\max}$ ($H_{\max}$ for magnetic fields), shown on top of each panel, allowing an improved interpretation of the static illustration of the oscillating fields.

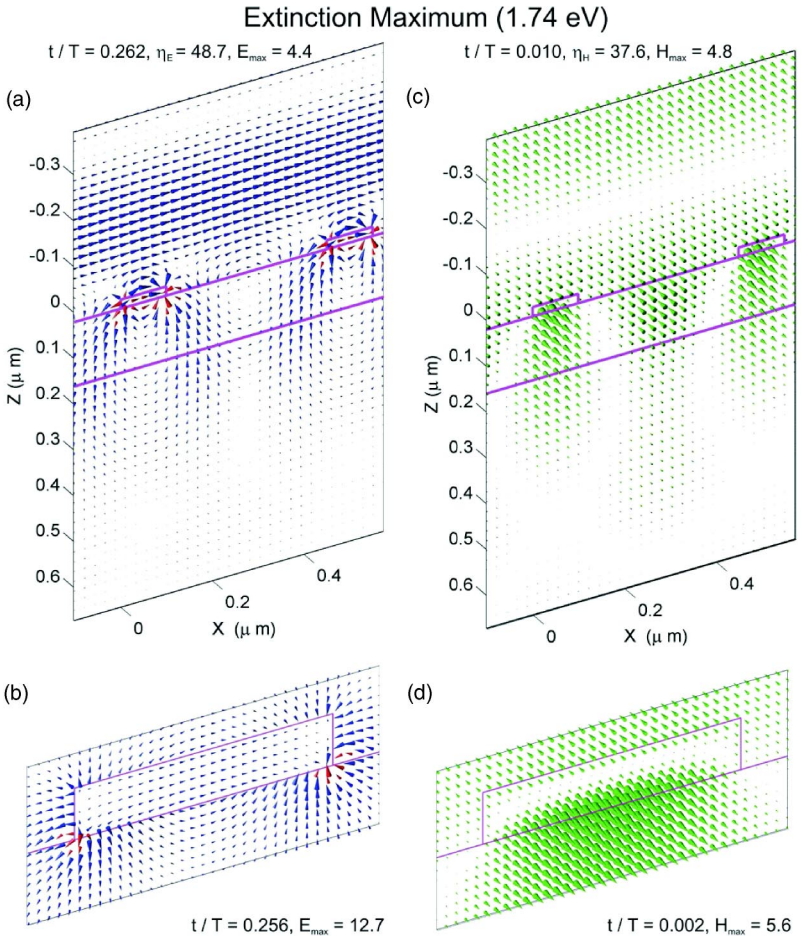

FIG. 13. (Color online) The calculated spatial distributions of the electric [blue and red cones in panels (a) and (b)] and magnetic [green cones in panels (c) and (d)] fields in a waveguiding structure with period $d_x=450$ nm, for normal incidence ($\vartheta=\varphi=0°$) and TM-polarized (across the wires) light. The fields are shown for an incoming photon energy of $\hbar\omega=1.74$ eV, corresponding to the 1st (lower energy) peak in extinction. The electric and magnetic fields are depicted at the moments of time t (measured in units of light period $T=2\pi/\omega$ and shown in the title of each panel) when the field intensities that are integrated over the displayed cross sections $\int_A \mathbf{E}^2 dA$ and $\int_A \mathbf{H}^2 dA$ reach maxima (see the explanation in the text). Solid magenta lines denote the cross-section of the structure. The incoming wave arrives from vacuum (at $z<0$). Panels (b),(d) show the fields in a magnified region around the gold nanowire. Red cones in panels (a),(c) are scaled by a multiplier of 0.5 in order to exclude the cones overlap in the regions of high electric fields near the sharp edges of the gold nanowire.

The first parameter t/T enables a direct derivation of temporal information. For example, the electric field is $\mathbf{E}(\mathbf{r},t)=\mathrm{Re}[\vec{\mathcal{E}}(\mathbf{r})\exp(-i\omega t)]$, where $\vec{\mathcal{E}}(\mathbf{r})=\vec{\mathcal{R}}(\mathbf{r})+i\vec{\mathcal{I}}(\mathbf{r})$. Then the electric field intensity integrated over the display area A is

$$W_E(t)=\int_A \mathbf{E}^2(\mathbf{r},t)dA=\overline{R_E^2}\cos^2(\omega t)+\overline{I_E^2}\sin^2(\omega t)+2\overline{R_E I_E}\sin(\omega t)\cos(\omega t), \tag{5}$$

where

$$\overline{R_E^2}=\int_A \vec{\mathcal{R}}^2(\mathbf{r})dA, \tag{6}$$

$$\overline{I_E^2}=\int_A \vec{\mathcal{I}}^2(\mathbf{r})dA,$$

$$\overline{R_E I_E}=\int_A \vec{\mathcal{R}}(\mathbf{r})\vec{\mathcal{I}}(\mathbf{r})dA.$$

Thus, $W_E(t)$ oscillates with frequency 2ω as

$$W_E(t)=\frac{1}{2}(\overline{R_E^2}+\overline{I_E^2})+\frac{1}{2}[(\overline{R_E^2}-\overline{I_E^2})^2+4\overline{R_E I_E}^2]^{1/2}\cos(2\omega t-\beta_E), \tag{7}$$

$$\beta_E=\arctan\frac{2\overline{R_E I_E}}{\overline{R_E^2}-\overline{I_E^2}}, \tag{8}$$

reaching its maximum value at $\omega t=\beta_E/2$ or $t/T=\beta_E/4\pi$, where $T=2\pi/\omega$ is the light period. For the magnetic field, the maximum of $W_H(t)$ is reached at $t/T=\beta_H/4\pi$, with respective changes in Eqs. (5)–(8). Note that the minima of W_E and W_H are reached a time span $T/4$ later. The corresponding calculated values of t/T are shown for each panel.

By comparing the values of t/T for electric and magnetic fields, the character of the light propagation (standing or propagating) at a particular frequency can be estimated. In the case of purely running character, and without averaging over spatial area, both maxima are reached simultaneously. In the case of a purely standing wave, there should be a $T/4$ delay between both, because the light energy oscillates between the electric and magnetic fields.

An additional important characteristic of the EM-field distribution given in Figs. 13 and 14 [panels (a) and (c)] is the field modulation coefficient,

$$\eta_E=\frac{W_{E,\max}}{W_{E,\min}}=\frac{\overline{R_E^2}+\overline{I_E^2}+[(\overline{R_E^2}-\overline{I_E^2})^2+4\overline{R_E I_E}^2]^{1/2}}{\overline{R_E^2}+\overline{I_E^2}-[(\overline{R_E^2}-\overline{I_E^2})^2+4\overline{R_E I_E}^2]^{1/2}} \tag{9}$$

(and the corresponding quantity η_H for the magnetic field). For example, the modulation coefficient η is on the order of one for purely running waves and diverges for purely stand-

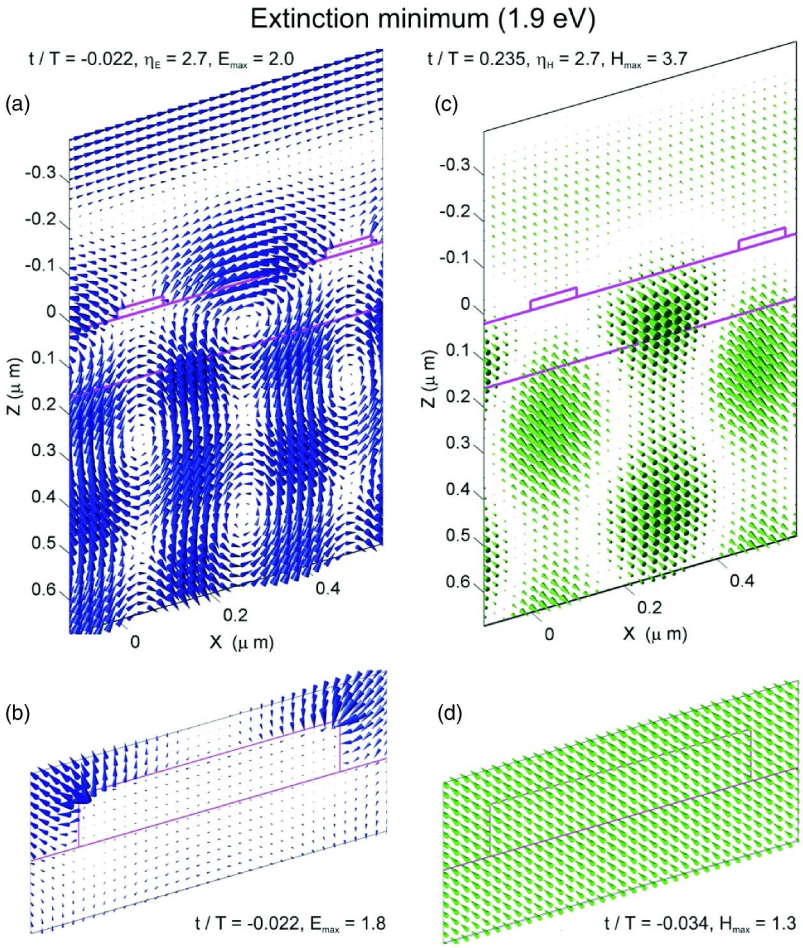

FIG. 14. (Color online) The calculated spatial distributions of the electric [blue and red cones in panels (a) and (b)] and magnetic [green cones in panels (c) and (d)] fields in a waveguiding structure with period $d_x = 450$ nm, for normal incidence ($\vartheta = \varphi = 0$) and TM-polarized (across the wires) light. The fields are shown for photon energy $\hbar\omega = 1.9$ eV, corresponding to the extinction minimum. All other rules for drawing this figure are the same as in Fig. 13.

ing waves, provided that the displayed cross-section A extends over several wavelengths along the wavevector direction.

Note that the fields of Fig. 13 and Fig. 14 are scaled by different coefficients. In order to compare the absolute magnitudes of the fields, we show in each panel the maximum absolute value of each field, $E_{\max}$ and $H_{\max}$, measured in units of the incoming field amplitudes. Additionally, the largest cones in panels (a),(b) of Fig. 13 (for the strongest electric fields near the gold nanowire edges) are shown in red and scaled by 0.5, to emphasize the regions of the largest field enhancement.

We would like to add here that the averaged characteristics of the near-field distributions t/T, η, $E_{\max}$, and $H_{\max}$ fluctuate with the mesh and cross-section A which is chosen to display the near-fields. However they provide an instructive qualitative information on the near-field distributions.

The case of the extinction maximum, which is depicted in Fig. 13, corresponds to a strongly standing character of the near-field. This follows from the high values of the field modulation ratios in panels (a),(c) of Fig. 13, $\eta_E \sim 50$ and $\eta_H \sim 40$. Compare these with the much smaller values in the case of extinction minimum, $\eta_E \sim \eta_H \sim 3$ in panels (a),(c) of Fig. 14.

The electric field is large and nearly homogeneous inside the wires and has a clearly dipolar character around the wires; see panel (b) in Fig. 13. These two features are characteristic for the dipolar plasmon resonance in subwavelength-size structures.

Another interesting feature can be noticed from a comparison between the electric and the magnetic field distributions inside the nanowires in panels (b),(d) of Fig. 13. Actually, it illustrates how the Maxwell equations work inside the metallic parts of the structure. First, the magnetic field is displayed approximately $1/4$ of the period earlier than the electric field. Second, panel (d) shows that the magnetic field changes its direction inside the wire, from negative to positive (i.e., along OY), approximately linearly with z. Thus,

$$\mathbf{H} \propto (0, z - z_0, 0) e^{-i\omega T/4} = (0, -i(z - z_0), 0),$$

where $0 < z_0 < L_z$ is inside the nanowire. From the Maxwell equation, rot $\mathbf{H} = (1/c)(\partial D/\partial t)$, and for a harmonic wave $\propto e^{-i\omega t}$, this means that induction in panel (b), i.e., $1/4$ of the period later than in panel (d), has to be

$$\mathbf{D} \propto (-1, 0, 0).$$

Therefore $\mathbf{D}$ has a direction opposite to OX and homogeneous along OZ. Because $\mathbf{D} = \varepsilon_{\text{gold}}\mathbf{E}$, and $\varepsilon_{\text{gold}} < 0$, this means that the electric field $\mathbf{E}$ has to be homogeneous across the wire and directed along OX. It is exactly what we see in panel (b).

Another exciting feature of the near-field distribution at the extinction maximum is a clearly visible horizontal standing wave inside the ITO layer. The important point is that this standing wave is pinned to the wires at the position of the anti-nodes (the field is maximum near the wire). The formation of this localized wave is due to the Bragg resonance of the two counter-propagating TM_0 guided modes with $k_{g,x}=\pm 2\pi/d_x$ as discussed above. This manifests itself by the predominant polarizations of the electric (perpendicular to the wire) and magnetic (along the wire) fields inside the ITO layer.

We can also see in Fig. 13 that the light does not propagate far into the substrate, which reveals the high extinction (simultaneous maxima of reflection and absorption).

In contrast to this situation for the extinction maximum, the electric field avoids the wire nearly completely in the case of high transmissivity (extinction minimum). As visible in Fig. 14, the distribution of the field inside the wire is still the same as in case of an extinction maximum, typical for a dipolar resonance. However, the amplitude of this dipolar field is one order of magnitude smaller. This follows from the fact that now the standing quasiguided wave in the ITO layer is pinned to the wires in another possible way, namely by its nodes. This explains actually the high transmissivity of the structure.

The fact that the wave is well transmitted through the structure is also clearly seen in Figs. 14(a) and 14(c). The strong modulation of the fields below the ITO layer occurs because the energy of the incoming light is above the Rayleigh anomaly, and two diffraction channels into the substrate are already opened. The interference between the transmitted and diffracted beams produces this clearly visible modulation.

The maximum values of the electric and magnetic fields, given in each panel in Figs. 13 and 14, allow us to estimate the degree of field enhancement in case of the resonance, and to compare it with the resonance Q-factor ($Q=\Omega/\Delta\Omega$, where Ω and $\Delta\Omega$ are the resonance energy and linewidth). For example, the quality factor of the lower energy resonance in Fig. 5(b) is $Q\sim 2.0\ \mathrm{eV}/0.1\ \mathrm{eV}\sim 20$, which gives the field enhancement factor $\sqrt{Q}\sim 5$. The latter is in agreement with the values of $E_{\max}$ and $H_{\max}$ specified in Figs. 13(a) and 13(c).

In order to conclude our discussion of the near-field distributions, we would like to emphasize that the near-field distribution analysis shows unambiguously that the electromagnetic field is resonantly increased at frequencies near the extinction maxima. It brings a clear additional evidence for the formation of a new quasiparticle, a waveguide-plasmon polariton, with energy dispersion manifesting itself via the extinction maxima (or, equivalently, transmission dips).

VI. CONCLUSIONS

In conclusion, we have shown experimentally and theoretically that far-field coupling effects can strongly influence the optical properties of gold nanowire gratings deposited on top of dielectric ITO layers. Our work clearly demonstrates that the transmission spectra of such photonic crystal structures can change substantially with the substrate thickness. While gold nanowire gratings on top of thinner ITO substrates, not supporting optical waveguide modes, only induce diffractive anomalies, structures on top of thicker waveguiding ITO layers can exhibit a much richer behavior. The transmission spectra of such structures are characterized by an additional sharp spectral feature due to the excitation of quasiguided modes of the corrugated waveguide. Strong coupling between these optical modes and the particle plasmon resonances of the nanowires results in the formation of a waveguide-plasmon polariton with a large Rabi splitting of nearly 250 meV. Scattering matrix theory gives an excellent agreement between all experimentally measured and theoretically modelled extinction spectra. Furthermore, we have shown that the scattering matrix formalism can be used to model the spatial distribution of the electromagnetic near-fields of the photonic crystal structure. The calculations reveal the existence of a standing wave inside the ITO layer below the gold nanowire gratings. In the case of strong coupling, this standing wave has field maxima at the position of the gold nanowires, leading to a large field enhancement near the wires and therefore high extinction values. The extinction minimum between the two polariton branches in contrast is due to a standing wave with anti-nodes between the nanowires and therefore only weak fields at the position of the gold nanowires.

ACKNOWLEDGMENTS

This work was financially supported by the German Bundesminister für Bildung und Forschung (FKZ 13N8340/1), the Deutsche Forschungsgemeinschaft (Priority Program SP1113), and in part by the Russian Foundation for Basic Research, the Russian Ministry of Science, and the Russian Academy of Sciences. The authors are grateful to K. von Klitzing for continuous support and to T. Ishihara, S. Linden, E. A. Muljarov, N. C. Nielsen, and V. V. Popov for discussions.

*Electronic address: a.christ@fkf.mpg.de

[1] E. Yablonovitch, Phys. Rev. Lett. **58**, 2059 (1987).

[2] S. John, Phys. Rev. Lett. **58**, 2486 (1987).

[3] J. D. Joannopoulos, R. D. Meade, and J. N. Winn, *Photonic Crystals* (Princeton University Press, Princeton, NJ, 1995).

[4] E. L. Ivchenko, A. Nesvizhskii, and S. Jorda, Phys. Solid State **36**, 1156 (1994).

[5] V. P. Kochereshko, G. R. Pozina, E. L. Ivchenko, D. R. Yakovlev, A. Waag, W. Ossau, G. Landwehr, R. Hellmann, and E. O. Göbel, Superlattices Microstruct. **15**, 471 (1994).

[6] M. Hübner, J. Kuhl, T. Stroucken, A. Knorr, S. W. Koch, R. Hey, and K. Ploog, Phys. Rev. Lett. **76**, 4199 (1996).

[7] L. Pilozzi, A. D'Andrea, and R. DelSole, Phys. Rev. B **54**, 10 763 (1996).
[8] T. Fujita, Y. Sato, T. Kuitani, and T. Ishihara, Phys. Rev. B **57**, 12 428 (1998).
[9] S. C. Kitson, W. L. Barnes, and J. R. Sambles, Phys. Rev. Lett. **77**, 2670 (1996).
[10] S. I. Bozhevolnyi, J. Erland, K. Leosson, P. M. W. Skovgaard, and J. M. Hvam, Phys. Rev. Lett. **86**, 3008 (2001).
[11] T. W. Ebbesen, H. J. Lezec, H. F. Ghaemi, T. Thio, and P. A. Wolff, Nature (London) **391**, 667 (1998).
[12] S. Linden, J. Kuhl, and H. Giessen, Phys. Rev. Lett. **86**, 4688 (2001).
[13] E. R. Brown and O. B. McMahon, Appl. Phys. Lett. **67**, 2138 (1995).
[14] E. Cubukcu, K. Aydin, E. Ozbay, S. Foteinopoulou, and C. M. Soukoulis, Nature (London) **423**, 605 (2003).
[15] A. Christ, S. G. Tikhodeev, N. A. Gippius, J. Kuhl, and H. Giessen, Phys. Rev. Lett. **91**, 183901 (2003).
[16] H. Raether, *Surface Plasmons on Smoth and Rough Surfaces and on Gratings* (Springer-Verlag, Berlin, 1988).
[17] J. G. Fleming, S. Y. Lin, I. El-Kady, R. Biswas, and K. M. Ho, Nature (London) **417**, 52 (2002).
[18] U. Kreibig and M. Vollmer, *Optical Properties of Metal Clusters* (Springer-Verlag, Berlin, 1995).
[19] T. Klar, M. Perner, S. Grosse, G. von Plessen, W. Spirkl, and J. Feldmann, Phys. Rev. Lett. **80**, 4249 (1998).
[20] C. Sönnichsen, T. Franzl, T. Wilk, G. von Plessen, J. Feldmann, O. Wilson, and P. Mulvaney, Phys. Rev. Lett. **88**, 077402 (2002).
[21] W. Rechberger, A. Hohenau, A. Leitner, J. R. Krenn, B. Lamprecht, and F. R. Aussenegg, Opt. Commun. **220**, 137 (2003).
[22] S. A. Maier, M. L. Brongersma, P. G. Kik, and H. A. Atwater, Phys. Rev. B **65**, 193408 (2002).
[23] B. Lamprecht, G. Schider, R. T. Lechner, H. Ditlbacher, J. R. Krenn, A. Leitner, and F. R. Aussenegg, Phys. Rev. Lett. **84**, 4721 (2000).
[24] H. R. Stuart and D. G. Hall, Phys. Rev. Lett. **80**, 5663 (1998).
[25] M. Nevière, in *Electromagnetic Theory of Gratings*, edited by R. Petit (Springer-Verlag, Berlin, 1980), Chap. 5, pp. 123–157.
[26] A. Hessel and A. A. Oliner, Appl. Opt. **4**, 1275 (1965).
[27] Another historically first example of the resonant Wood anomaly are the surface plasmons anomalies in periodically corrugated metallic layers (Ref. 40). A lot of research is connected with these anomalies, see, e.g., in Ref. 41. In the current paper, however, we restrict ourselves to structures with isolated metal nanowires, where such plasmons do not manifest themselves, unless a periodic modulation along the wires is included.
[28] S. G. Tikhodeev, A. L. Yablonskii, E. A. Muljarov, N. A. Gippius, and T. Ishihara, Phys. Rev. B **66**, 045102 (2002).
[29] C. D. Ager and H. P. Hughes, Phys. Rev. B **44**, 13 452 (1991).
[30] D. M. Whittaker and I. S. Culshaw, Phys. Rev. B **60**, 2610 (1999).
[31] P. B. Johnson and R. W. Christy, Phys. Rev. B **6**, 4370 (1972).
[32] P. Lalanne and G. M. Morris, J. Opt. Soc. Am. A **13**, 779 (1996).
[33] G. Schider, J. R. Krenn, W. Gotschy, B. Lamprecht, H. Ditlbacher, A. Leitner, and F. R. Aussenegg, J. Appl. Phys. **90**, 3825 (2001).
[34] C. L. Haynes, A. D. McFarland, L. Zhao, R. P. V. Duyne, G. C. Schatz, L. Gunnarsson, J. Prikulis, B. Kaesemo, and M. Käll, J. Phys. Chem. B **107**, 7337 (2003).
[35] M. K. Barnoski, *Introduction to Integrated Optics* (Univ. of Calif., Santa Barbara, 1973), Chap. 3, pp. 53–72.
[36] R. Shimada, A. L. Yablonskii, S. G. Tikhodeev, and T. Ishihara, IEEE J. Quantum Electron. **38**, 872 (2002).
[37] A. L. Yablonskii, E. A. Muljarov, N. A. Gippius, S. G. Tikhodeev, T. Fujita, and T. Ishihara, J. Phys. Soc. Jpn. **70**, 1137 (2001).
[38] C. Weisbuch, M. Nishioka, A. Ishikawa, and Y. Arakawa, Phys. Rev. Lett. **69**, 3314 (1992).
[39] U. Neuberth, N. Rau, M. Wegener, S. Linden, S. Pereira, K. Busch, A. Christ, and J. Kuhl, *International Symposium on Photonic and Electromagnetic Crystal Structures V*, Tu-P6, Kyoto, Japan, 2004.
[40] R. H. Ritchie, E. T. Arakawa, J. J. Cowan, and R. N. Hamm, Phys. Rev. Lett. **21**, 1530 (1968).
[41] W. L. Barnes, A. Dereux, and T. W. Ebbesen, Nature (London) **424**, 824 (2003).